A Data-Driven Reflectance Model

Wojciech Matusik [*]   Hanspeter Pfister [†]   Matt Brand[†]   Leonard McMillan [‡]

Figure 1: Renditions of materials generated using our model: steel teapot with greasy fingerprints (left), teapot with rust forming (right). Closeup pictures in the center. We used a spatially varying texture to interpolate between reflectance models for each point on the teapot.

Abstract

We present a generative model for isotropic bidirectional reflectance distribution functions (BRDFs) based on acquired reflectance data. Instead of using analytical reflectance models, we represent each BRDF as a dense set of measurements. This allows us to interpolate and extrapolate in the space of acquired BRDFs to create new BRDFs. We treat each acquired BRDF as a single high-dimensional vector taken from a space of all possible BRDFs. We apply both linear (subspace) and non-linear (manifold) dimensionality reduction tools in an effort to discover a lower-dimensional representation that characterizes our measurements. We let users define perceptually meaningful parametrization directions to navigate in the reduced-dimension BRDF space. On the low-dimensional manifold, movement along these directions produces novel but valid BRDFs.

Keywords: Light Reflection Models, Photometric Measurements, Reflectance, BRDF, Image-based Modeling

1 Introduction

A fundamental problem of computer graphics rendering is modeling how light is reflected from surfaces. A class of functions called

[*]MIT, Cambridge, MA.
Email: wojciech@graphics.lcs.mit.edu
[†]MERL, Cambridge, MA.
Email: [pfister,brand]@merl.com
[‡]UNC, Chapel Hill, NC.
Email: mcmillan@cs.unc.edu

Bidirectional Reflectance Distribution Functions (BRDFs) characterizes the process where light transport occurs at an idealized surface point.

Traditionally, physically inspired analytic reflection models [Cook and Torrance 1982] [He et al. 1991] [He et al. 1992] provide the BRDFs used in computer graphics. These BRDF models are only approximations of reflectance of real materials. Furthermore, most analytic reflection models are limited to describing only particular subclasses of materials – a given model can represent only the phenomena for which it is designed. Significant efforts have been expended on improving these models by incorporating the relevant aspects of the underlying physics. Many of these models are based on material parameters that in principle could be measured, but in practice are difficult to acquire.

An alternative to directly measuring model parameters is to acquire actual samples from a BRDF using some version of a gonio-spectro-reflectometer [Marschner et al. 2000] [Cornell] [CUReT] [STARR] [Dana 2001] [Ward 1992] and then fit the measured data to a selected analytic model using various optimization techniques [Ward 1992] [Yu et al. 1999] [Lafortune et al. 1997] [Lensch et al. 2001]. There are several shortcomings to this measure-and-fit approach. First, a BRDF represented by the analytic function with the computed parameters is only an approximation of real reflectance; measured values of the BRDF are usually not exactly equal to the values of the analytic model. The measure-and-fit approach is often justified by assuming that there is inherent noise in the measurement process and that the fitting process filters out these errors. This point of view, however, ignores more significant modeling errors due to approximations made in the analytic surface reflection model. Many of the salient and distinctive aspects of an objects reflection properties might lie within the range of these modeling errors. Second, the choice of the error function over which the optimization should be performed is not obvious. For example, error based on the Euclidean distance is a poor metric since it tends to overemphasize the importance of the specular peaks (these are usually much higher than the rest) and ignore the off-specular values. Finally, there is no guarantee that the optimization process will yield the best model. Since most BRDF models are highly non-linear, the optimization frameworks used in the fitting process rely heavily on initial guesses of the models parameters. The quality of these initial guesses can have a dramatic impact on the final

parameter values of the model.

Another approach is to acquire dense measurements of the BRDF and use these measurements directly in the rendering process. This approach preserves those subtleties of the measured data that are lost in a data-fitting approach. However, it is time-consuming since it requires reflectance measurements for all desired materials in the scene. Furthermore, we end up with a collection of measured BRDFs and not with a parameterized reflectance model. Any change to the material property would require finding a real material with the desired property and acquiring its reflectance.

We suggest an alternative sampling-based approach for modeling surface reflectance. We capitalize on the fact that it is feasible to rapidly acquire accurate reflectance measurements using image-based techniques. We acquire BRDFs for a large representative set of materials. Materials in our collection include metals, paints, fabrics, minerals, synthetics, organic materials, and others. We introduce a new approach to BRDF modeling, an approach that is data driven – it interpolates/extrapolates new BRDFs from the representative BRDF data. Our approach has the advantage that the produced BRDFs look very realistic since they are based on the measured BRDFs. Furthermore, we provide a set of intuitive parameters that allow users to change the properties of the output BRDF. We also let users specify their own parameters by labeling a few representative BRDFs. We believe that this way of specifying model parameters makes our model much easier to use and control than the analytic models in which the meaning of parameters is often non-intuitive [Pellacini et al. 2000].

In our model, we do not want to store all acquired BRDFs explicitly. This leads us to the analysis of the space of all possible BRDFs for common materials in the world. A BRDF for these materials is not an arbitrary function, and we seek a representation for all possible functions corresponding to physical BRDFs. We treat each of our acquired BRDFs as a single high-dimensional vector where each measurement is an element of this vector. Then we apply both linear and non-linear dimensionality reduction tools to obtain a low dimensional manifold that characterizes the set of BRDFs we measured. In the process we also obtain a mapping between the embedding manifold and the original BRDF space. Therefore we can always compute the corresponding BRDF for each point on the manifold. An interesting side effect of our approach is that it suggests an inherent dimensionality for the space of all isotropic BRDFs.

To summarize, the main contributions of this paper are:

- We introduce a novel model for an isotropic BRDF that is based on measured reflectance for a large set of materials.

- We introduce a set of perceptually-based parameters for this model. We also let users specify their own parameters.

- We analyze both linear and non-linear dimensionality of the space of isotropic BRDFs.

- In our model the parameter values are pre-defined for many typical materials – the materials we have measured. Using our model we can also generate difficult to represent effects such as rust, oxidation, or dust.

2 Previous Work

The value of physically accurate reflectance models has long been understood within the computer graphics community [Blinn 1977]. The availability of BRDF models based on the actual physics of light transport and validated by empirical measurements were a significant catalyst in this realization [Torrance et al. 1966] [Trowbridge and Reitz 1975]. Physical accuracy was an impetus behind the development of many subsequent computer graphics reflection

models [Cook and Torrance 1982][He et al. 1991]. An interesting transition occurred with [Ward 1992], when Ward developed a BRDF model that, while not strictly physically based, was capable of describing most significant reflection phenomena. He went to great effort to ensure that his model obeyed the most basic of physical laws (reciprocity and energy conservation), and significantly, he fit his model's parameters to actual material measurements. More recently, the availability of low-cost digital cameras has rekindled interest in BRDF acquisition and modeling. One particularly ambitious undertaking is the CUReT BRDF database [Dana et al. 1999] [CUReT]. The CUReT database represents approximately 200 reflectance measurements over varying incident and reflected angles for a planar patch of 60 different materials. With a uniform material sample this amounts to a relatively sparsely sampled BRDF. Such a sparsely sampled BRDF is not directly useful as a table-based BRDF function; thus, it was necessary to fit an analytic function in order to get a useful model.

Marschner [Marschner et al. 2000] constructed another significant BRDF measurement system. His system, although limited to only isotropic BRDF measurements, was both fast and robust. In particular, his system took unique advantage of reciprocity, bilateral symmetry, and multiple simultaneous measurements to achieve unprecedented leverage from each reflection measurement. This offers a significant advantage. It filters measurement noise due to minute variations over the surface, errors due to spatial variations in photosite response within the image sensor, and variations in illumination intensity. In the face of such statistical averaging, one is hard pressed to attribute the inevitable residual errors that occur when model fitting to additional systematic noise, rather than failings of the analytic model.

The inherent dimensionality of a BRDF, combined with the desire to sample it at high resolutions in order to model specular, incident, and retroreflection effects, leads to an unwieldy sampling and storage problem. Many researchers have addressed this specific problem by searching for a more appropriate basis for representing BRDFs. Spherical harmonics [Westin et al. 1992] and spherical wavelets [Schröder and Sweldens 1995] are natural choices for representing the angular parameters of the BRDF. Other efficient representations include wavelets [Lalonde and Fournier 1997], Zernicke polynomials [Koenderink et al. 1996],and separable approximations obtained using singular value decomposition [Kautz and McCool 1999] or a purely positive matrix factorization [McCool et al. 2001]. Furthermore, recent image-based approaches to BRDF modeling [Lensch et al. 2001] have demonstrated the power of using linear combinations of a compact reflectance function basis sets for modeling spatially varying BDRFs. Such linear decompositions lead to an interesting question: can the true space of potential BRDFs be described as a linear combination of basis functions? Clearly, factorizations of the sort used to compress BRDFs are linear, allowing for arbitrary mixtures of their basis vectors to fit a given set of data. If this decomposition approach were in fact valid, it would imply that linear combinations of actual BRDFs might be used to model original and physically plausible reflection models. Exploring the ramifications of this hypothesis is one of our motivations for developing a sample-based generative model.

3 Data Acquisition

In order to acquire a sufficient number of adequately sampled BRDFs, it was necessary to build a measurement device. Our modeling approach placed two requirements on the acquired data: first, that each BRDF be sampled densely enough that it could be used directly as a table-based model, and second, that the space of BRDFs be sampled adequately so as to span the range of models that we hope to generate. Accordingly, we have built a BRDF measurement device suitable for rapidly acquiring high-quality BRDFs for a wide

Figure 2: A photograph of our high-speed BRDF measurement gantry.

range of different materials (see Figure 2). The image-based BRDF measurement device described by [Marschner et al. 2000] inspired our design.

Our acquisition system requires a spherically homogenous sample of the material. The system is placed in a completely isolated room painted in black matte. It consists of the following components: a QImaging Retiga 1300 (a 10 bit, and a 1300x1030 resolution Firewire camera), a Kaidan MDT-19 (a precise computer-controlled turntable), and a Hamamatsu SQ Xenon lamp (a lamp with stable light emission output and a continuous and relatively constant radiation spectrum over the visible light range). The lamp is mounted on an arm to the turntable. The light orbits the measurement sample placed at the center of rotation; the camera is stationary. Our camera is geometrically calibrated using the technique described in [Zhang 1998]. The position of the light source is determined using a contact digitizer (FARO Arm). We use the same digitizer to determine the position of the center of the material sample. The radius of the sample is measured with calipers. The light source moves in increments of approximately $0.5°$ from the point exactly opposite the camera (the sample is in between the camera and the light source) to the point exactly in front of the camera. We take a total of 330 high dynamic range pictures to cover the required half circle. This process takes about 3 hours. For each high dynamic range picture we take a total of 18 10-bit photographs. The exposure time ranges from 40 microseconds to 20 seconds. We use the fact that our CCD camera has a very linear response curve to derive the high dynamic measurement. For each pixel in the image we fit a line to the exposure time vs. radiance values. The slope of the line is used as the radiance estimate. The correlation of this line is higher than 0.998.

Each acquired image of the sample sphere represents many BRDF samples. Essentially each pixel of the sphere is treated as a separate BRDF measurement. In order to compute the specific BRDF value for a given pixel we perform the following steps. First, we intersect the ray defined by the pixel with the sphere to determine point P. Then, we compute the normal at point P on the sphere, the vector and the distance to the light source, and the vector to the camera pixel. Next, we compute the irradiance at point P due the light source (taking into account distance to the light source and foreshortening). Finally, we compute the BRDF value as the ratio of the high dynamic range radiance to the irradiance.

4 Data Representation

We found that specular peaks were difficult to represent using the natural coordinate system $(\theta_{in}, \theta_{out}, \phi_{diff})$. Even when binning a BRDF at a dense grid (every $1°$ spacing for each dimension), it is not possible to reproduce original images (the specular highlight becomes an oval shape, oriented at different directions). We use a different coordinate system, described in [Rusinkiewicz 1998] and shown in Figure 3. This coordinate frame is based on the angles with respect to the half-angle (half-vector between incoming and outgoing directions). This coordinate frame allows us to vary the sampling density near the specular highlight. Specifically, we vary θ_h (angle between the normal and the half-vector), assigning smaller bins for values near specular reflection and larger bins for angles far away from the specular reflection.
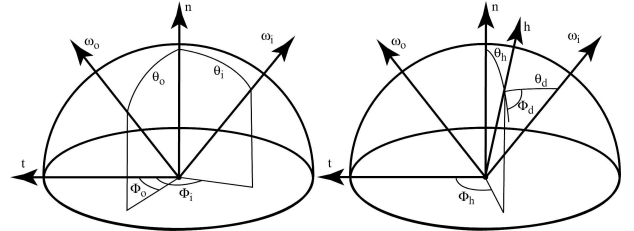

Figure 3: The standard coordinate frame is shown on the left. Rusinkiewicz's coordinate system is shown on the right.

We still discretize θ_h, θ_d into 90 bins and ϕ_d into 360 bins. This results in a total of 90 x 90 x 360 = 2,916,000 bins for each color component. We halve this number to 1,458,000 by enforcing the reciprocity constraint:

$$f(\theta_h, \theta_d, \phi_d) = f(\theta_h, \theta_d, \phi_d + \pi) \qquad (1)$$

With this constraint we need only to discretize ϕ_d into 180 bins.
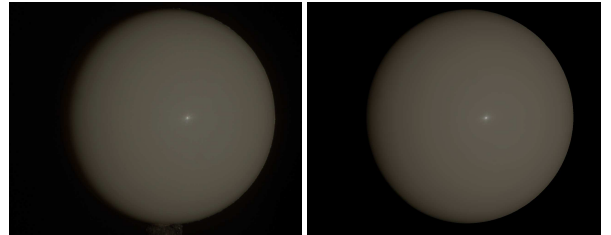

Figure 4: Two log images of a sphere (alumina oxide). A real image is shown on the left. A synthesized image using tabulated BRDF data is shown on the right.

Our measurement process gives us typically 20-80 million BRDF samples for each material. We reduce the noise in our measurements by removing the outliers in each bin (lowest and highest 25% of the values), and we average the remaining measurements. This statistical smoothing is intended to remove systematic noise as well as compensate for small variations in material properties over the sample. As a final validation we render a synthesized version of our sample sphere and compare it to the corresponding acquired high dynamic range image. We conduct this inspection for all input light configurations. Pictures for a typical acquired material are in shown in Figure 4. The rendered images reproduce the input images very well. We have used our device to acquire BRDF measurements of more than 130 different materials, including metals, plastics, painted surfaces, and cloth. Figure 5 depicts some of the materials that were sampled. We have removed from further analysis some materials that exhibited significant subsurface scattering, anisotropy, or non-homogenity.
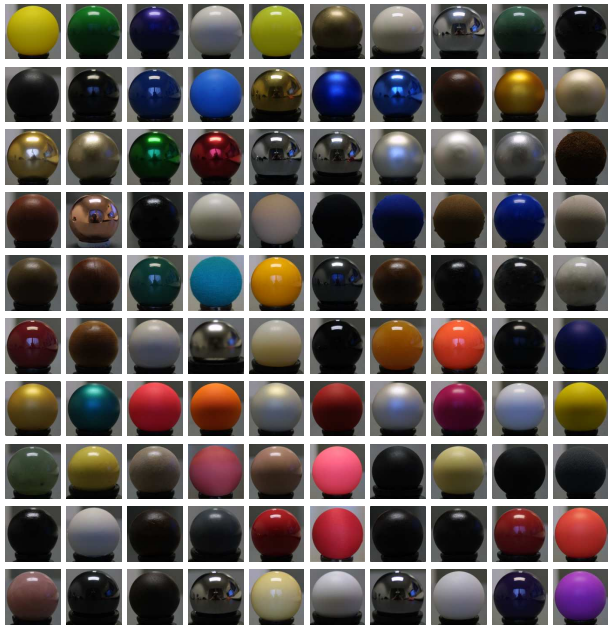
Figure 5: Pictures of 100 of our acquired materials.

5 Data Analysis

These sampled BRDFs can be used directly by a renderer. Several examples of that are shown in Figure 6, where a teapot is rendered under natural illumination using the raw acquired data. Our ultimate goal, however, is to construct an empirical BRDF model that can be used to generate novel, yet plausible, reflectance functions directly from this database. We begin with the following assumption: if we treat each of our BRDF samples as a high dimensional vector in an abstract BRDF space, we expect that all physical BRDFs lie upon a lower dimensional manifold within this space indicative of their inherent dimensionality. This is a common assumption used by others [Cula and Dana 2001] and it is consistent with the relatively small number of parameters seen in analytic BRDF models. Therefore, we breakdown the task of constructing an empirical BRDF model into two phases: discovering this lower dimensional model, and defining an interpolation scheme within this lower-dimensional subspace.

5.1 Linear Analysis

In the case where the physical BRDF manifold lies on a linear subspace, the analysis tools for both manifold discovery and interpolation are well known. In this case, Principal Component Analysis (PCA)[Bishop 1995] effectively determines a set of basis vectors that span the desired subspace, and linear combinations of samples can be used for interpolation. Linear manifold approaches have proven extremely effective in some problem domains, such as face synthesis [Blanz and Vetter 1999] and radiance interpolation [Chen et al. 2002]. Potential linear manifolds are generally suggested when there is a noticeable plateau in the magnitudes of the sorted eigenvalues. When this plateau occurs on the kth eigenvalue, we can model the data as a k-dimensional linear subspace with a residual error bounded by the square root of the sum of the squares of the remaining eigenvalues.

We began our analysis of the BRDF samples by searching for a linear embedding manifold (a hyperplane). The three color channels of each BRDF sample were assembled into a column vector and concatenated to form a 4,374,000 by 104 measurement vector matrix X.

Figure 6: Rendered teapots using BRDFs from our database: nickel, hematite, gold paint, and pink fabric.
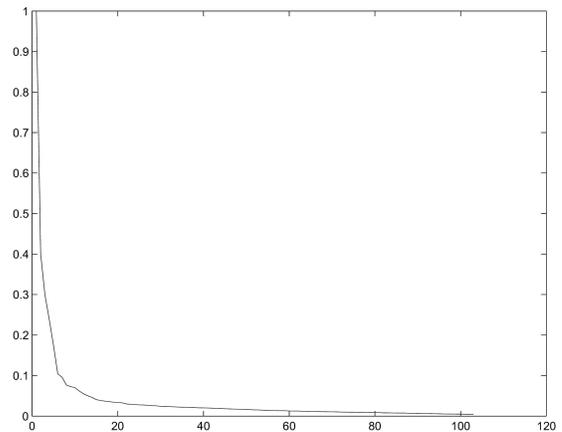

Figure 7: Plot of the eigenvalues resulting from PCA of the data set.

We perform the analysis in the log space (we apply the natural logarithm to each element of vector X). There are several reasons for this normalization. First, there is a huge difference (on the order of a few magnitudes) between the specular and non-specular values of the BRDF. If used in the original space, the analysis tools would associate more importance to noise in the specular values than the actual non-specular components. The linear analysis would depreciate importance of these non-specular values (the non-specular values are perceptually important). Our operation is also justified by the fact that the human visual system is sensitive to ratios rather than absolute radiance values.

Singular value decomposition was then applied to $X^T X$ (a 104x104 matrix). The singular values in this case are the squares of the desired eigenvalue magnitudes. A plot of these eigenvalues is shown in Figure 7. We also show in Figure 8 the reconstruction of a typical material using first 1, 5, 10, 20, 30, 45, 60, and all principal components. We see that good reconstruction is usually obtained using the first 30-40 components.

While there is a considerable fall off in the sequential values seen in this plot, the plateau is reached around 45th eigenvalue (the reconstruction error is about 1% at that point). This dimension of the embedding subspace is considerably higher than our intuition would suggest, based on the typical number of parameters used in analytic BRDF models. We verified that the 45-dimensional space defined by the first principal components reconstructs all our measured BRDFs well. However, it spans a space that is bigger than the space of all possible BRDFs. We are able to find the points in this
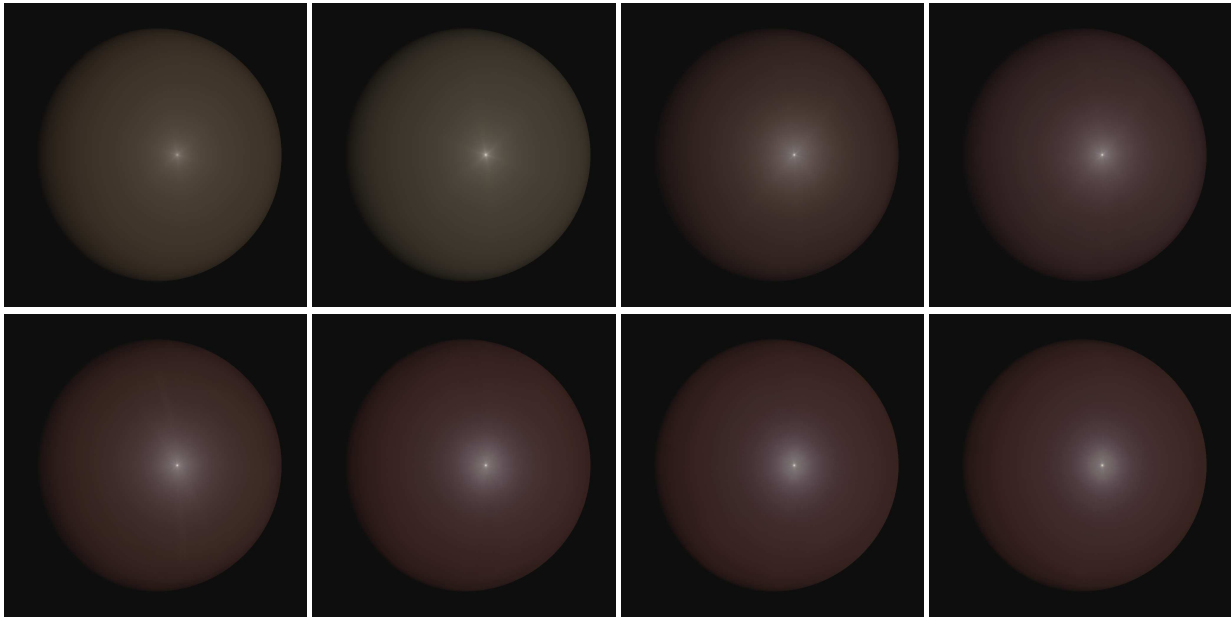
Figure 8: Reconstruction of a BRDF from principal components in the order of increasing number of components – mean, 5, 10, 20, 30, 45, 60, and all.

subspace that do not correspond to any physical materials. In other words, using linear combinations of the components, we can obtain the data samples that do not look like BRDFs. We illustrate this point in Figure 9. Moreover, in order to span the whole space, we would need to have at least 45 parameterization directions in order to reach all specified BRDFs. This suggests that the space of all possible BRDFs lies on a lower-dimensional manifold that is non-linearly embedded in the 45D linear space. In the next section, we apply recently developed nonlinear dimensionality reduction techniques to discover this lower dimensional manifold.

5.2 Nonlinear dimensionality reduction

Nonlinear dimensionality reducers (NLDR) compute low-distortion embeddings of high-dimensional data in low-dimensional target spaces. The nonlinearity usually obtains from the fact that only local relationships in the ambient space are preserved while long-distance relationships are presumed to be corrupted by the curvature of the manifold in the ambient space. First-generation NLDRs such as nonmetric MDS [Kruskal and Wish 1978], IsoMap [Tenenbaum et al. 2000], and LLE [Roweis and Saul 2000] generalize PCA to give low-dimensional embeddings of the data, but offer no mapping of the data points. Recently, two second-generation methods have been announced that offer continuous mappings between the embedding an the original (ambient) space: Automatic Alignment [Teh and Roweis 2003] combines LLE with a set of pre-estimated local dimensionality reducers–each of which is presumed to be fitted to a relatively flat subset of the manifold–and solves for a mixture of these projections that globally flattens the data while minimizing barycentric distortion in each point neighborhood. Charting [Brand 2003] solves for a kernel-based mixture of projections that minimizes Euclidean distortion of local neighborhoods; it includes a solution for the local dimensionality reducers needed by automatic alignment. We chose to use charting because it is explicitly designed to work well with small numbers of samples and to suppress measurement noise, two conditions that tend to break methods for dimensionality reduction from local relationships.

Figure 10 gives the main geometric intuition behind charting. First one solves for a set of flat "pancake" Gaussians that smoothly
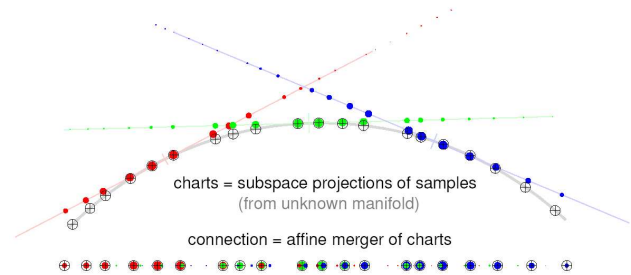

Figure 10: A simple charting example. Points ($\oplus$) sampled from a unknown manifold (gray curve) are projected onto three subspaces (red, green, and blue lines) and assigned a probability (indicated by size) according to their distance from the point where the chart touches the manifold. A minimal-distortion merger of these charts gives a flattening of the manifold in a lower dimensional space, where the mapped locations of points are the probability-weighted combinations of their chart-specific locations.

cover the data manifold, in the sense that adjoining Gaussians have similar orientation. The dominant axes of each Gaussian specify a subspace. Projecting the data into this subspace gives a "chart" of one part of the manifold. A chart preserves local structure where it touches the manifold and suppresses measurement noise that displaces samples off the manifold. A data point has a location and a probability in every chart. Due to curvature of the manifold, a chart gives a very distorted picture of faraway points; these points are assigned very low probability.

The pancake Gaussians are solved under a criterion that optimizes the charts for the ensuing "connection." The connection is an affine merger of all charts in the target space–effectively a flattening of the manifold that minimally distorts all charts and maximizes agreement between overlapping charts of the locations of points to which they assign high probability. The connection gives
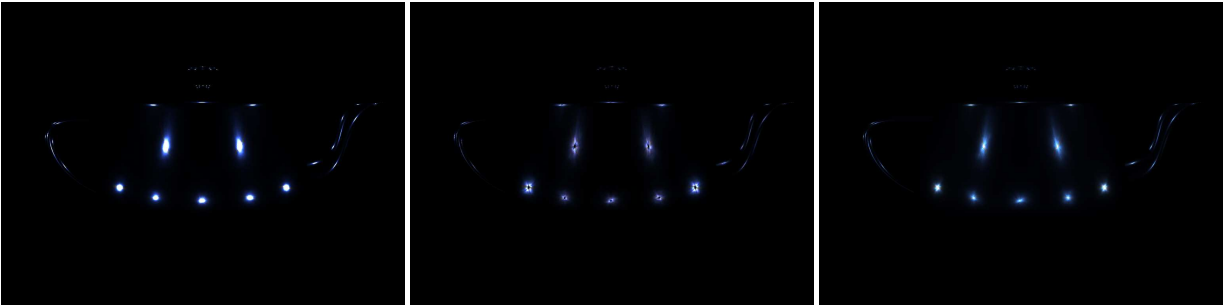
Figure 9: Nonlinear spaces generate valid BRDFs where linear spaces fail. Original BRDF corresponding to a point A on a 45 dimensional hyperplane (left). Physically implausible reflectance (hole in the middle of the specular highlight) corresponding to moving away from a point A on the 45 dimensional linear subspace (center). Physically plausible reflectance corresponding to moving equally far away from point A on the 15 dimensional non-linear manifold (right).
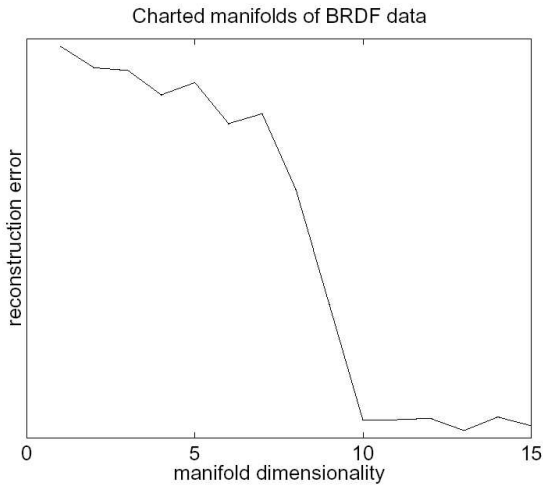

Figure 11: Data reconstruction error as a function of the dimensionality of the global chart. The sharp drop in this error curve indicates that a 10-dimensional chart is sufficient for the BRDF data. In fact, that chart has a better reconstruction error than a 25-dimensional PCA.

mappings between the ambient and target spaces, which are simply mixtures of affine projections, weighted by the probability that a point "belongs" to each chart. The dimensionality-reducing mapping from the ambient to the target space effectively imposes a low-dimensional coordinate system on the samples, while the inverse mapping gives a smoothly curving low-dimensional surface in the ambient space, effectively reconstructing the original manifold.

For charting, one must specify a set of chart centers, a width parameter σ for the Gaussians, and a target dimensionality d. We used the default settings: one chart centered on each data point and σ = half the average distance between each point and its closest neighbor. Note that locating a chart on a point does not cause the manifold to pass through that point–only near it. See [Brand 2003] for additional details.

As with PCA, the data-reconstruction error of a charted data set gives an indication of the true dimensionality of the manifold. Figure 11 shows that our BRDF data probably lies on a 10D manifold. The reconstruction error does not decline monotonically because each dimensionality may merit a different flattening. For example, if the data were sampled from a truncated cone, the best 1D chart would simply be height along the cone, while the best 2D chart

would flatten the cone into an annulus. Each flattening would suppress the noise in different directions, some more fortuitous than others.

While the 10D manifold exhibits good reconstruction of the original data, our goal is to synthesize novel BRDFs. With that in mind we chose to work on a 15D manifold because interpolations on it pass even closer to the data density (with error comparable to 45D PCA reconstruction). Moreover, this dimensionality is roughly consistent with previous isotropic BRDF models [Ward 1992], [Lafortune et al. 1997], and [Koenderink et al. 1996], which have at least 10 degrees of freedom.

A charted manifold of BRDF data makes it possible to treat the space of BRDFs as if it were linear, and to identify meaningful axes of variation in this embedding space. An interpolating or extrapolating line in this space is a nonlinear curve in the original BRDF space that passes closer to the data density that the equivalent straight line would (on average), simply because it stays on the manifold where a straight line does not. This translates directly to superior BRDF synthesis, as will be demonstrated below.

6 Model Construction

In order to use our sample-based reflectance model it is necessary to develop intuitive user interfaces for specifying and exploring new materials. We investigated methods for characterizing material traits by analogies derived from the existing samples. We believe that such methods provide the best and most intuitive user interface [Pellacini et al. 2000].

Our model is built from actual physical measurements and it reproduces these measurements. Therefore, we have defined model parameters for a large collection of materials – materials we have measured. We believe that the most useful scheme of navigation is when users can choose as a starting point some type of the material similar to the one they desire. In our case they can pick any of the measured materials. Then, they would change the reflectance properties of this material according to one of the following schemes (these navigation schemes are applicable for both linear and nonlinear manifold models). The simplest method is to choose another BRDF and move in this direction. Although of limited use, this method works well for perceptually similar materials.

A more useful approach is to define directions corresponding to a desired trait (the parameterization direction is a 45D vector for linear space and a 15D vector for nonlinear space). We pick some arbitrary point on the manifold and then move in the direction defined by the vector by adding it to the current position to increase the trait, or subtracting it to decrease the trait. We can backproject the current point onto the original BRDF space to check the corresponding BRDF. Next, we describe various procedures for identi-

fying trait vectors.

Our modeling approach requires the user to specify a sufficient set of traits. This specification can be as simple as a binary classification (i.e., noting whether each acquired BRDF has the specified trait.) We also allow the user to leave a BRDF unspecified in cases where the trait is hard to determine or simply does not apply. Usually the more samples we specify for each class the more precise the direction is.

There are many different ways to define the parameterization directions based on the classification. We have examined and evaluated a few. (A) Mean difference [Blanz and Vetter 1999]: In this approach we compute the average of each BRDF in each complementary pair of clusters associated with a trait (i.e., those samples with, and those without) in the embedding space. Then the vector between these complement averages in the embedding space is the parameterization direction. This direction vector is then applied (added or subtracted) to the current point in the embedding space. (B) Support vector machines [Vapnik 1995]: Support vector machines determine the hyperplane which separates the data points in the first material class from the data points in the second class. The partitioning hyperplane has maximum distance to the closest points (called support vectors) in both material classes. The parameterization direction is the normal to this hyperplane. The hyperplane is defined in 15D space for non-linear analysis and 45D for the linear space. This method also tells us on which side of the hyperplane the current point is, and how far the point is from the plane. (C) Fisher's linear discriminant [Duda and Hart 1973]: Each material class corresponds to a some distribution of high-dimensional data (15D for non-linear analysis and 45D for linear analysis). Fisher's linear discriminant defines a projection of these distributions on the axis such that the distributions projected on this axis are the most separable (the projection maximizes the distance between the means of the two classes while minimizing the variance of each class). In practice, support vector machines performed the best on our data set and Fisher's linear discriminant performed the poorest.

Since we want our model to preserve the basic principles of physics, we have to disallow movements on the manifold that do not adhere to these principles. We consider the three following principles:

- Reciprocity: As mentioned before, reciprocity in our model is met by default since we store only half of the BRDF vector.

- Non-negativity: We allow the user to move only in the space so that all the values in the backprojected vector are positive.

- Energy conservation: A unit of light energy is applied at some incoming light direction. If the sum of energy in all outgoing directions is less than one (we assume that the surface does not emit energy by itself) then the energy is conserved. This has to be true for all incoming light directions in order for a BRDF to follow energy conservation. We enforce this and do not allow the users to produce BRDFs for which the sum of energy for any incoming direction is greater than one.

7 Results

Once the BRDFs are acquired and validated, as described in section 4, we performed both linear and non-linear dimensionality reduction as described section 5. We then set out to construct a perceptual BRDF model using the techniques outlined in section 6. This section presents the results from a typical model construction session.

A test subject was asked to characterize each of the BRDFs from our database using 16 different traits. These included *redness*, *greenness*, *blueness*, *specularness*, *diffuseness*, *glossiness*,
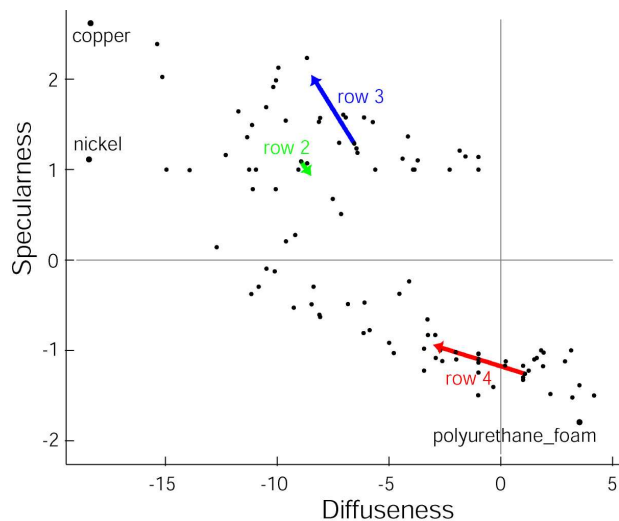

Figure 12: *Diffuseness* trait vs *specularness* trait. Observe that the *diffuseness* and *specularness* traits exhibit a weak inverse correlation. The green, blue, and red vectors denote projections of the BRDF interpolations shown in the second, third, and fourth rows of Figure 16 respectively.
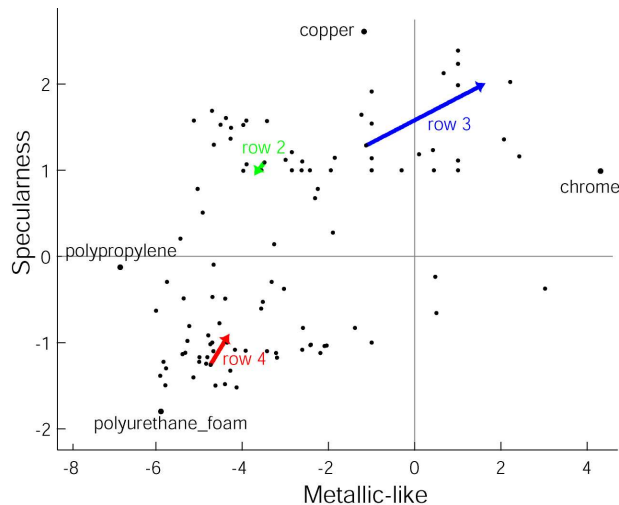

Figure 13: *Metallic-like* trait vs *specularness* trait. Observe that the *metallic-like* and *specularness* traits exhibit a weak correlation. The green, blue, and red vectors denote projections of the BRDF interpolations shown in the second, third, and fourth rows of Figure 16 respectively.

metallic-like, *plastic-like*, *roughness*, *silverness*, *gold-like*, *fabric-like*, *acrylic-like*, *greasiness*, *dustiness*, *rubber-like*. In a sense, these parameters are arbitrary since the classification is completely based on the subject's interpretation. We could have chosen traits without physical connotations, such as *ugly* or *pleasing*. Alternatively, the traits could have been based on actual measurable quantities, such as conductivity and mean surface variation. Our test subject characterized each BRDF as one of three choices: 1) possessing the particular trait, 2) not possessing the trait, or 3) unclear. We then used the subject's characterizations to build a model in both the linear and non-linear embedding spaces using Support Vector Machines.

The results from this trait-based analysis are shown as projections onto the derived trait vectors in Figures 12, 13, and 14. These projections are computed in the linear embedding space given by

our non-linear model. Observe that the metallic and specular characteristics are weakly correlated, the specular and diffuse traits are weakly inverse-correlated, and the glossy and diffuse traits are inverse-correlated. This is what we would expect. Note that we do not make attempts to model independent traits in either our trait selection or trait vector derivations. Therefore, we expect that addition of a particular trait to an existing BRDF may effect other traits. This lack of parameter independence is a tradeoff that we accept in order to establish perceptually meaningful parameters in our modeling approach. Despite the fact that the parameterization vectors are not orthogonal, they did span the whole 15D non-linear embedding space and provide an intuitive set of "dials" for users to design materials.
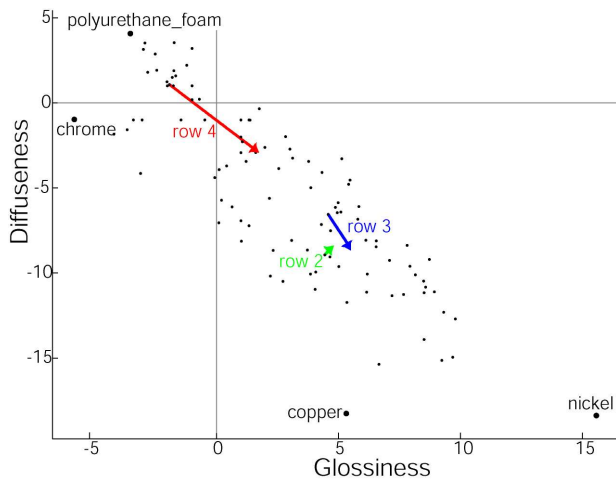

Figure 14: *Glossiness* trait vs *diffuseness* trait. Observe that the *glossiness* and *diffuseness* traits exhibit an inverse correlation. The green, blue, and red vectors denote projections of the BRDF interpolations shown in the second, third, and fourth rows of Figure 16 respectively.

Once trait vectors are established, we can add and subtract them from our data points in our embedding space. In Figure 15 we demonstrate four examples of varying user-specified traits using the linear model. The first row shows a teapot rendered using our *Gold-Paint* BRDF on the far left, and the effect of adding the *redness* trait in successive steps to the right. The second row starts from a our *SpecularGold* BRDF (left) with successive additions of the *silverness* trait. The third row adds the *gold-like* trait to the *Blue-GlossyPaint* BRDF (left). Finally, the fourth row shows the addition of the *specularness* trait to the *BlackMattePlastic* BRDF. It is our experience that the linear model gives reasonable BRDFs if only small displacements are permitted. If the displacement is too large, physically invalid BRDFs result (as illustrated in Figure 9).

We then applied the same trait classifications and Support Vector Machine calculations to the embedding space of our non-linear model. Figure 16 demonstrates 4 examples using this approach. The first row of Figure 16 shows our *Copper* BRDF on the left, with successive additions of the *roughness* trait. The second row begins with our *GreenAcrylic* BRDF and shows the addition of the *blueness* trait. The trajectory of this path is also illustrated in Figures 12, 13, and 14. Notice that color-change specification is not particularly correlated with any of traits used for these projections. Thus, we would expect relatively small movements and no preferred direction. The third row, on the other hand, represents the addition of the *metallic* trait to the *VioletAcryllic* BRDF model, whose path is also illustrated in the projections in Figures 12, 13, and 14. The path trajectory of this example conforms to our expectations, and its magnitude is large in these visualizations since the

metallic trait is correlated to the *glossiness* and *specularness* traits used as axis. The fourth row starts with *YellowDiffusePaint* BRDF and shows the addition of the *glossiness* trait, which is depicted as the red path in Figures 12, 13, and 14. The direction of this path is as we would expect, and it has a large magnitude due to the fact the the *YellowDiffusePaint* BRDF is located far away from the glossy examples in the projections shown.

Overall the non-linear basis set results in a more robust model than our linear basis set, in that we were able to move large distances within the non-linear embedding space and still generate physically plausible BRDFs with the expected appearance.

Our modeling approach also allows us to associate approximate trait vectors with physical processes. This can be done in one of two ways, by fitting a least-squares line to a path of specified BRDFs in the embedding space, or by computing local piecewise difference vectors between examples. As an example, we have modeled metal oxidation. We measured the reflectance changes as a metal was exposed to an acidic environment. It changed from highly specular polished material to black matte material. The acquired four BRDFs determine a path in the embedding space. The intermediate stages are interpolated in the embedding space and backprojected to the sample space (Figure 17). Figure 1 illustrates another process – rust formation. We used a spatially varying texture to select *rust* levels for each point on the teapot. We are currently measuring more processes like this such as copper patination and other types of rust formation.

8 Future Work and Conclusions

In this paper we have introduced a new approach for modeling isotropic BRDFs. Our model generates new surface reflectance models by forming combinations from a set of densely-sampled, acquired BRDFs. We are hopeful that data-driven reflectance modeling approaches, like ours, can greatly expand the range of material models used in computer graphics rendering.

In order to develop an effective and efficient interpolation scheme we choose to first analyze the inherent dimensionality of our data set. To this end we applied both in linear subspace and nonlinear manifold analysis. The results of this analysis are suggestive of the overall structure of BRDFs. Specifically, we found that the linear subspace model lent itself to the creation of physically implausible BRDFs, and a large number of dimensions (around 45) were required to adequately represent our measurements. Nonetheless, we still found the linear subspace model to be useful for interpolation over small distances. The nonlinear model, on the other hand, was much more compact in its dimensionality (around 14 dimensions for the same accuracy as the 45-dimension linear subspace model), and more robust in its ability to interpolate plausible BRDFs over long distances. However, we caution against over generalizing from our results. We are comfortable in saying that our modeling approach effectively represents our data set, but our sample size is still relatively small to draw conclusions regarding the fundamental nature of isotropic BRDFs. However, we are optimistic that techniques like ours can be used to greatly expand our knowledge in these areas.

We also have demonstrated methods for defining intuitive parameters for navigating within BRDF models. These techniques can easily be customized for a range of industrial and artistic applications. Furthermore, they can be personalized for individual use or made objective by incorporating physical measurements.

The advantages of our data-driven BRDF model include a high degree of realism, a perceptually meaningful parameterization, relative ease of modeling for complex surface materials, and speed of evaluation. The main disadvantage of the model is its size. We believe that the model we propose can easily be incorporated into existing rendering systems. We also hope to extend our

Figure 15: Navigation in the linear space. Each row corresponds to changing one parameter of the model. The first row shows an increase in the *redness* trait applied to the *GoldPaint* BRDF. The second row illustrates an increase in the *silverness* trait applied to the *SpecularGold* BRDF. Row three applies the *gold-like* trait to the *BlueGlossyPaint* BRDF. The fourth row shows an increase in the *specularness* trait applied to the *BlackMattePlastic* BRDF.

work in sample-based reflectance modeling to include anisotropy (4D BRDF), macro-scale surface variations typically described by BTFs, and subsurface scattering effects (BSSRDF). Another obvious extension would be to use this model in solving inverse rendering problems.

9 Acknowledgments

References

BISHOP, C. M. 1995. *Neural Networks for Pattern Recognition*. Clarendon Press.

BLANZ, V., AND VETTER, T. 1999. A morphable model for the synthesis of 3D faces. *Computer Graphics 33*, Annual Conference Series, 187–194.

BLINN, J. 1977. Models of light reflection for computer synthesized pictures. *Computer Graphics 11*, Annual Conference Series, 192–198.

BRAND, M. 2003. Charting a manifold. In *To appear, Proc. NIPS-15*.

CHEN, W.-C., BOUGUET, J.-Y., CHU, M. H., AND GRZESZCZUK, R. 2002. Light Field Mapping: Efficient Representation and Hardware Rendering of Surface Light Fields. *ACM Transactions on Graphics 21*, 3 (July), 447–456. ISSN 0730-0301 (Proceedings of ACM SIGGRAPH 2002).

COOK, R., AND TORRANCE, K. 1982. A reflection model for computer graphics. *ACM Transactions On Graphics 1*, 1 (January), 7–24.

CORNELL. Light Measurement Laboratory. Web page. http://www.graphics.cornell.edu/ research/measure/.

CULA, O. G., AND DANA, K. 2001. Compact representation of bidirectional texture functions. In *Proc. of Computer Vision and Pattern Recognition*, in press.

CURET. Columbia-Utrech Reflectance and Texture. Web page. http://www.cs.columbia.edu/ CAVE/curet/.

DANA, K. J., VAN GINNEKEN, B., NAYAR, S. K., AND KOENDERINK, J. J. 1999. Reflectance and texture of real world surfaces. *ACM Transactions on Graphics 1*, 18, 1–34.

DANA, K. 2001. BRDF/BTF measurement device. *ICCV*, 460–466.

DUDA, R. O., AND HART, P. E. 1973. *Pattern Classification and Scene Analysis*. Wiley-Interscience Publication, New York.

HE, X., TORRANCE, K., SILLON, F., AND GREENBERG, D. 1991. A comprehensive physical model for light reflection. *Computer Graphics 25*, Annual Conference Series, 175–186.

Figure 16: Navigation on the non-linear manifold. Each row corresponds to changing one parameter of the model. The first row shows an increase in the *roughness* trait applied to the *Copper* BRDF. The second row illustrates an increase in the *blueness* trait applied to the *GreenAcrylic* BRDF. Row three applies the *metallic-like* trait to the *VioletAcryllic* BRDF. The fourth and fifth rows show an increase in the *glossiness* trait applied to the *YellowDiffusePaint* BRDF (the images in the fifth row are the enlarged versions of the first and last image in the fourth row).

Figure 17: Progression of the steel oxidation process. Our BRDF model also supports interpolation along physically meaningful path. In this example we start with a completely polished steel sample (upper left) and progressively oxidize it. The final black-oxidized sample is shown on the lower right.

HE, X., HEYNEN, P., PHILLIPS, R., TORRANCE, K., SALESIN, D., AND GREENBERG, D. 1992. A fast and accurate light reflection model. *Computer Graphics 26*, Annual Conference Series, 253–254.

KAUTZ, J., AND MCCOOL, M. 1999. Interactive rendering with arbitrary BRDFs using separable approximations. In *Rendering Techniques '99 (Proceedings of the Tenth Eurographics Workshop on Rendering)*, Springer Wien, New York, NY, 281–292.

KOENDERINK, J., VAN DOORN, A., AND STAVRIDI, M. 1996. Bidirectional Reflection Distribution Function expressed in terms of surface scattering modes. *European Conference on Computer Vision*.

KRUSKAL, J. B., AND WISH, M. 1978. *Multidimensional Scaling*. Sage Publications, Beverly Hills, CA.

LAFORTUNE, E., FOO, S.-C., TORRANCE, K., AND GREENBERG, D. 1997. Non-linear approximation of reflectance functions. *Computer Graphics 31*, Annual Conference Series, 117–126.

LALONDE, P., AND FOURNIER, A. 1997. A wavelet representation of reflectance functions. *IEEE Transactions on Visualization and Computer Graphics 3*, 4, 329–336.

LENSCH, H., KAUTZ, J., GOESELE, M., HEIDRICH, W., AND SEIDEL, H.-P. 2001. Image-based reconstruction of spatially varying materials. In *Proceedings of the 12th Eurographics Workshop on Rendering*, 104–115.

MARSCHNER, S., WESTIN, S., LAFORTUNE, E., AND TORRANCE, K. 2000. Image-based measurement of the Bidirectional Reflection Distribution Function. *Applied Optics 39*, 16.

MCCOOL, M., ANG, J., AND AHMAD, A. 2001. Homomorphic factorization of BRDFs for high-performance rendering. *Computer Graphics 35*, Annual Conference Series, 171–178.

PELLACINI, F., FERWERDA, J., AND GREENBERG, D. 2000. Toward a psychophysically-based light reflection model for image synthesis. *Computer Graphics 34*, Annual Conference Series, 55–64.

ROWEIS, S. T., AND SAUL, L. K. 2000. Nonlinear dimensionality reduction by locally linear embedding. *Science 290* (December 22), 2323–2326.

RUSINKIEWICZ, S. 1998. A new change of variables for efficient BRDF representation. In *Rendering Techniques '98 (Proceedings of Eurographics Rendering Workshop '98)*, Springer Wien, New York, NY, G. Drettakis and N. Max, Eds., 11–22.

SCHRÖDER, P., AND SWELDENS, W. 1995. Spherical wavelets: Efficiently representing functions on the sphere. *Computer Graphics 29*, Annual Conference Series, 161–172.

STARR. NIST reference reflectometer: STARR facility. Web page. http://physics.nist.gov/Divisions/Div844/facilities/brdf/starr.htm.

TEH, Y. W., AND ROWEIS, S. T. 2003. Automatic alignment of hidden representations. In *To appear, Proc. NIPS-15*.

TENENBAUM, J. B., DE SILVA, V., AND LANGFORD, J. C. 2000. A global geometric framework for nonlinear dimensionality reduction. *Science 290* (December 22), 2319–2323.

TORRANCE, K., SPARROW, E., AND BIRKEBAK, R. 1966. Polarization, directional distribution, and off-specular peak phenomena in light reflected from roughened surfaces. *Journal of the Optical Society of America 56*, 7 (July), 916–925.

TROWBRIDGE, T., AND REITZ, K. 1975. Average irregularity representation of roughened surfaces. *Journal of the Optical Society of America 65*, 5, 531–536.

VAPNIK, V. 1995. *The Nature of Statistical Learning Theory*. Springer, N.Y.

WARD, G. 1992. Measuring and modeling anisotropic reflection. *Computer Graphics 26*, Annual Conference Series, 265–273.

WESTIN, S., ARVO, J., AND TORRANCE, K. 1992. Predicting reflectance functions from complex surfaces. *Computer Graphics 26*, Annual Conference Series, 255–264.

YU, Y., DEBEVEC, P., MALIK, J., AND HAWKINS, T. 1999. Inverse global illumination: Recovering reflectance models of real scenes from photographs. In *Computer Graphics*, SIGGRAPH 99 Proceedings, 215–224.

ZHANG, Z. 1998. A flexible new technique for camera calibration. Tr98-71, MSR Redmond.